Physical and observational constraints on the anvil cloud area feedback

Brett A. McKim[a,b], Sandrine Bony[a], & Jean-Louis Dufresne[a]

Abstract Changes in anvil clouds with warming remain a leading source of uncertainty in estimating the Earth's climate sensitivity. Here, we develop a novel feedback analysis that decomposes changes in anvil clouds and creates testable hypotheses for refining their proposed uncertainty ranges with observations and theory. To carry out this storyline approach, we derive a simple but quantitative expression for the anvil area feedback, which is shown to depend on the present day, measurable cloud radiative effects and the fractional change in anvil area with warming. Satellite observations suggest an anvil cloud radiative effect of about ± 1 Wm^{-2}, which requires the fractional change in anvil area to be about $\mp 50\%$ K^{-1} to produce a feedback equal to the current best estimate of its lower bound. We use quantitative theory and observations to show that the change in anvil area is closer to about -4% K^{-1}. This constrains the area feedback and leads to our new estimate of 0.02 ± 0.07 $\mathrm{Wm}^{-2}\mathrm{K}^{-1}$, which is many times weaker and more constrained than the overall anvil cloud feedback. In comparison, we show the anvil cloud albedo feedback to be much less constrained, both theoretically and observationally, and thus to embody the uncertainty that poses an obstacle for bounding the Earth's climate sensitivity.

THE severity of global warming depends on how sensitive the Earth's surface temperature is to increased CO_2 (1, 2). Determining the precise sensitivity hinges on constraining the cloud response to warming (3). While recent progress has been made in constraining low cloud feedbacks (4, 5), anvil cloud feedbacks remain a large source of uncertainty (1, 2) despite decades of study (6–12). Anvil clouds pose a particular challenge because their radiative balance results from large, opposing radiative effects (13). Is this balance guaranteed? Or will warming tip the scales?

Uncertainty in anvil cloud feedbacks It has long been thought that anvil clouds might produce a strong negative climate feedback—first by functioning as a shortwave *tropical thermostat* (6), however the observations that led to this conclusion are no longer considered evidence of such an effect (7); then as a longwave *infrared iris* (8). Criticisms of this latter study's methodology soon followed (9, 14, 15), but they did not rule out the existence of a strong anvil cloud feedback.

Comprehensive assessments still consider changes in anvil clouds to be a leading source of uncertainty in estimates of climate sensitivity (1, 2). These assessments refer to an uncertain *anvil cloud area* (or *amount*) *feedback*, but it is more accurate to regard it as the *altitude-corrected anvil cloud feedback* (hereafter referred to as the *anvil cloud feedback*) since it results from changes in both area and optical depth, but not altitude changes which are considered in a separate feedback (16). The question of which individual feedback—area or optical depth—truly embodies the uncertainty remains unanswered. They must be separated to determine which is the main obstacle to constraining Earth's climate sensitivity.

Anvil cloud area is controlled in part by unconstrained microphysics (17–19), but also by robust thermodynamic principles (20, 21). These principles predict that anvils decrease in area with warming because the static stability of the atmosphere increases (21), which is consistent with observed variability (22–24) and with most simulations (25). The resulting area feedback *might* be small because anvils are radiatively neutral (7, 11, 26). But how neutral must anvil clouds be for their area feedback to be insignificant? What if their radiative effect changes with warming? And what if when anvils shrink, more of the Earth is exposed to the radiative effects and feedbacks of underlying low clouds? Such questions have thus far limited our ability to constrain the anvil cloud area feebdack.

Less is known about how cloud optical depth changes with warming, but it will manifest in optical properties such as the anvil cloud's albedo. Changes in albedo might produce an even stronger feedback than changes in area because anvils have a much stronger effect in the shortwave than in the net (11). But how much does cloud albedo change with warming? And how much must it change to produce a substantial feedback? Such questions persist and so we cannot yet conclude whether this feedback is more uncertain than the other.

Clearing the cloud of uncertainty A physically-motivated decomposition that accounts for cloud overlap and other confounding factors and distinguishes the feedbacks from changes in anvil area and albedo is needed. Since models must contend with representing unconstrained microphysics (17–19), we will primarily use observations. This rules out the use of purely model-based cloud feedback decompositions (27, 28). A cloud controlling factor analysis, an observational-based method mostly used for constraining low cloud feedbacks (29), requires further investigation before being suitable for constraining anvil cloud feedbacks with confidence. The connection between anvil clouds and the cloud controlling factors of the large-scale environment are not as well understood as in the case of low clouds.

Here, we derive a novel analytical cloud feedback decomposition based on the essential physics of cloud radiative effects. When combined with observations, this decomposition lets us

Compiled on 6 December 2023
[a] LMD/IPSL, Sorbonne Université, CNRS, 75252 Paris, France
[b] University of Exeter, Stocker Rd, EX4 4PY Exeter, UK

identify, understand, and quantitatively constrain cloud feedbacks in a physically transparent way. We adopt a *storyline approach* (30), in which we examine the driving factors that control a cloud feedback and judge the plausibility of these factors to produce a particular feedback value by using observations of clouds and theory based on process understanding. This approach shows which feedback is constrained and which is the obstacle to constraining climate sensitivity.

Conceptualizing cloud radiative effects

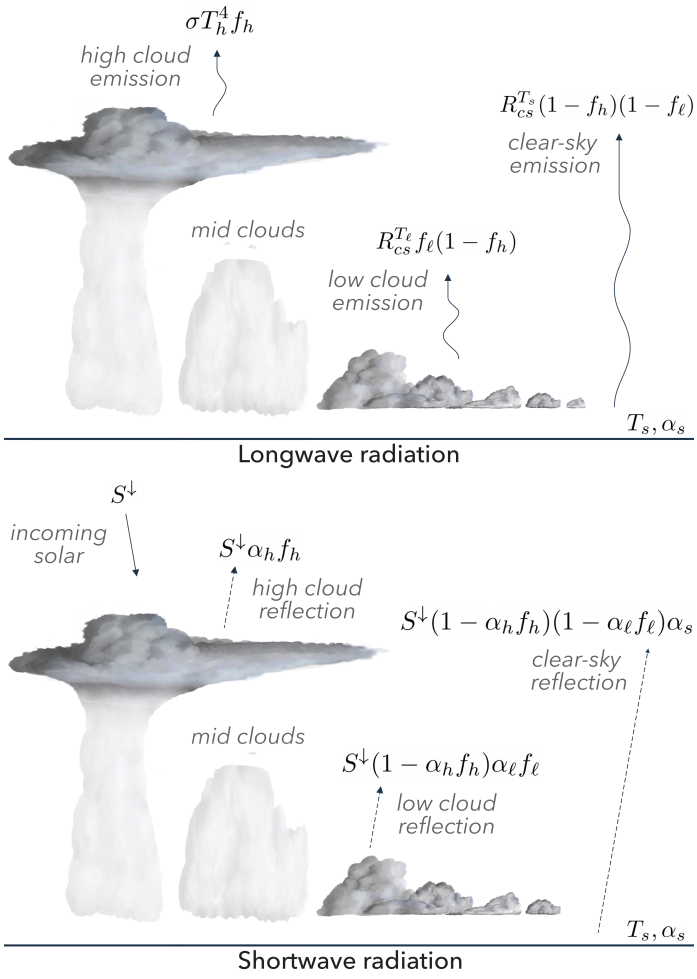

Figure 1: *Conceptualizing cloud radiative effects.* We idealize the vertical cloud profile into two distinct layers that represent anvil clouds and low clouds with random overlap. Equations indicate the domain-averaged contribution of high clouds, low clouds, and the surface to TOA energy balance. Their sum in the longwave and shortwave is given by Equation 14 and 16, respectively. See Table 1 for symbol meanings and values.

Clouds are complex, but for simplicity we divide them into two types: high (h) and low (ℓ). We subsume their properties into a few bulk parameters that can be obtained from observations and reanalysis (Table 1). These properties include their area fraction f_h, f_ℓ, their emission temperature T_h, T_ℓ, and their cloud albedo α_h, α_ℓ. Longwave emissivity will not be considered because most clouds have an emissivity close to one (31). Clear-sky radiation can also be distilled into a few parameters: the incoming solar radiation $S^\downarrow$, the surface albedo α_s, and the outgoing longwave radiation for a given surface temperature $R_{\text{cs}}^{T_s}$. Neglecting atmospheric absorption will bias the surface and cloud albedos to be higher than they would otherwise be, but this simplification permits the derivation of analytical expressions for cloud radiative effects from high clouds and low clouds C_h, C_ℓ; cloud overlap effects $m_{\ell h}$; and the TOA energy balance N. See Figure 1 for an illustration and Methods for the derivation. We will revisit some of these assumptions when discussing cloud albedo feedbacks

Analytic feedbacks and the storyline approach

Feedbacks are computed by differentiating Earth's TOA energy balance (Equation 16 minus Equation 14, see Methods) with respect to the surface temperature T_s (32). To start, we have:

$$\lambda \equiv \frac{dN}{dT_s} = \frac{dN_{\text{cs}}}{dT_s} + \frac{dC}{dT_s}, \tag{1}$$

where N_{cs} is the clear-sky TOA energy balance and $C = C_h + C_\ell + m_{\ell h}$ is the net cloud radiative effect from all clouds. Plugging in the analytical expressions for C (Equation 15 and 17, see Methods), we arrive at an equation for tropical climate feedbacks in terms of our bulk parameters:

$$\lambda = \lambda_0 + \sum_{i=h,\ell} \left(\lambda_i^{\text{area}} + \lambda_i^{\text{temp}} + \lambda_i^{\text{albedo}} \right), \tag{2}$$

where λ_0 is the reference response assuming a fixed anvil temperature and fixed relative humidity (12, 33); and λ_i^{area}, λ_i^{temp}, $\lambda_i^{\text{albedo}}$ are the feedbacks from changes in cloud area, cloud temperature, and cloud albedo with warming. All feedbacks are described analytically. See Methods for the full derivation.

These analytic expressions form the basis of our storyline approach by transparently and quantitatively relating changes in cloud properties to their resulting radiative feedbacks. A more formal Bayesian framework of hypothesis testing (used in 1, 30 to constrain climate sensitivity by reconciling diverse lines of evidence) will not be necessary here because we primarily consider a process understanding of the changes in anvil cloud area and do not need to reconcile other lines of evidence.

The anvil cloud area feedback Let us first focus on the high cloud area feedback, λ_h^{area}. After collecting all terms from Equation 1 that involve changes in anvil area df_h/dT_s, we arrive at a remarkably simple equation for the anvil cloud area feedback,

$$\lambda_h^{\text{area}} = \frac{d \ln f_h}{dT_s} \left(C_h + m_{\ell h} \right). \tag{3}$$

It depends on the *fractional* change in anvil area with warming $d \ln f_h / dT_s$ and the sum of the *present day* anvil cloud radiative effect C_h and cloud overlap effect $m_{\ell h}$. The logarithmic derivative is used because fractional changes in cloud area are easier to interpret and bound than absolute changes—as we will soon see. And though we computed the change in cloud radiative effect with warming, our physically-based decomposition shows the area feedback does not depend on the change in radiative effect, but its present-day value. This means it can be quantified and used to constrain the feedback.

The storyline approach in a nutshell Equation 3 reveals that the smaller the climatological anvil cloud radiative effect, the larger the change in anvil area would have to be to produce a given feedback strength. Therefore, we can probe the plausibility of a particular strength by first quantifying the observed anvil cloud radiative effect; then calculating the change in anvil area required to produce such a feedback strength; and then comparing the required change in anvil area to the amount expected from theory, simulations, and observations. If the expected change in anvil area is much smaller than the required change, then that particular feedback strength can be ruled out.

Climatology

Bounding the area feedback requires quantifying the tropically averaged anvil cloud radiative effect and cloud overlap effect ($C_h + m_{\ell h}$). Since these quantities are not directly observed, they will be inferred from our simple model of cloud radiative effects.

We do this by inputting observations of cloud fraction from CALIPSO (34), clear-sky radiation from CERES (35), surface temperature from HadCRUT5 (36), and atmospheric temperature from ERA5 reanalysis (37) into our expression for the net cloud radiative effect (Equations 15 and 17), see Methods. Similar to (22), f_h and f_ℓ are identified as the maximum of the observed cloud fraction profile above and below 8 km, respectively, and for an optical depth range between 0.3 and 5. This definition excludes the thickest and thinnest portion of anvil clouds, but the relationship between cloud area and surface warming is robust to the optical depth range considered (22).

We then ensure goodness of fit between the inferred and the observed cloud radiative effects by adding a single scaling factor n to the anvil cloud fraction, which accounts for collapsing the anvil cloud fraction profile into a single level (Methods and Extended Data Figure 1). We treat n as a constant because spatio-temporal variations in the *vertical* profile of anvil clouds affect the optical depth and hence α_h and α_ℓ, which already capture this variability as they are allowed to vary from year-to-year. In summary, we treat n, α_h, and α_ℓ as tuneable parameters to ensure consistency with observations at TOA (see Methods for further details).

We test our idealizations by comparing the observed net, shortwave, and longwave cloud radiative effects (C_{obs}, $C^{\text{sw}}_{\text{obs}}$, $C^{\text{lw}}_{\text{obs}}$) with their counterparts from the simple model (Figure 2), which take the spatial fields of cloud fraction, temperature, albedo, and clear-sky radiation as inputs. Our model can reproduce the spatial patterns of longwave and shortwave cloud radiative effects, although there are small deviations throughout the tropics, such as an underestimate of C in the south east of China and an overestimate of C in the eastern Pacific, next to South America (Figure 2c). Given the overall close agreement, we consider our model fit for the task of evaluating the tropical anvil cloud area feedback.

The climatological values of tropical quantities used in our calculations are summarized in Table 1 of Extended Data and the cloud properties of interest are plotted in Figure 3. f_h is maximum in the West Pacific Warm Pool and f_ℓ is maximum along the East Pacific. Decomposing C into its contributions from different layers reveals that the net C is dominated by C_ℓ. By comparison, the overlap effect $m_{\ell h}$ is much smaller and varies less. The same is true for the high cloud radiative effect C_h, which exhibits a remarkable cancellation between its shortwave and longwave components not just in the warm pool (13, 24, 38), but across the tropics.

Constraining the anvil cloud area feedback

With these more precise values in hand, we can constrain the tropical anvil cloud area feedback. To scale our estimate of λ_h^{area} to the global average, we multiply by the area ratio of the tropics and the globe, $1/2$.

$$\langle \lambda_h^{\text{area}} \rangle = \frac{1}{2} \frac{d \ln f_h}{dT_s} \Big(C_h + m_{\ell h} \Big). \tag{4}$$

The plausible lower bound on $\langle \lambda_h^{\text{area}} \rangle$ at present is $-0.4\,\text{Wm}^{-2}\text{K}^{-1}$, which comes from assuming all the magnitude in the anvil cloud feedback in (1) is due to area changes alone. This lower bound allows the possibility of an overall negative cloud feedback, a necessary ingredient for a climate sensitivity below 1.5 K (30). Our inferred value tropical mean value of $C_h + m_{\ell h} \approx -1.5$ Wm^{-2} implies that $d \ln f_h / dT_s$ must be $\approx 50\%$ K^{-1} to achieve this feedback strength.

Following our storyline approach, we will assess how plausible these cloud changes are by comparing them to the changes expected from the stability iris hypothesis assuming a moist adiabat (21) and from observed interranual variability (22).

Changes in anvil area with warming The stability iris hypothesis (21) states that anvil cloud fraction f_h is proportional to detrainment from deep convection. Owing to mass conservation, this detrainment is equal to the clear-sky convergence, $\partial_p \omega$, where ω is the subsidence vertical velocity [hPa day^{-1}]. If we make the ansatz that $\partial_p \omega$ is proportional to ω at the level of detrainment (h), then the fractional change in anvil area is equal to the fractional change in subsidence velocity at the anvil level:

$$\frac{d \ln f_h}{dT_s} = \frac{d \ln \omega_h}{dT_s}. \tag{5}$$

The subsidence velocity can be written as the quotient of the clear-sky radiative flux divergence in temperature coordinates ($-\partial_T F$) and the difference between the actual and dry lapse rates (19):

$$\omega = \frac{-\partial_T F}{1/\Gamma - 1/\Gamma_d}. \tag{6}$$

Given that $\partial_T F$ does not vary with surface temperature (39), if we further assume that Γ_h, the lapse rate at the anvil level, is moist adiabatic, then the change in cloud area can be computed with a few representative numbers. Assuming the surface warms from $T_s = 298$ K to 299 K and the anvil cloud warms from $T_h = 221$ K to anywhere between 221 and 221.4 K (a typical range of anvil warming, see 40 and references therein), then we expect that anvils change in area at about

$$\begin{aligned} \frac{d \ln f_h}{dT_s} &= -\frac{d \ln(1/\Gamma_h - 1/\Gamma_d)}{dT_s} \quad \text{(stability iris)} \\ &\approx -1 \text{ to } -4\%\ \text{K}^{-1}, \end{aligned} \tag{7}$$

depending on the amount of anvil warming. Despite the numerous simplifications in our derivation, the result is similar to the mean

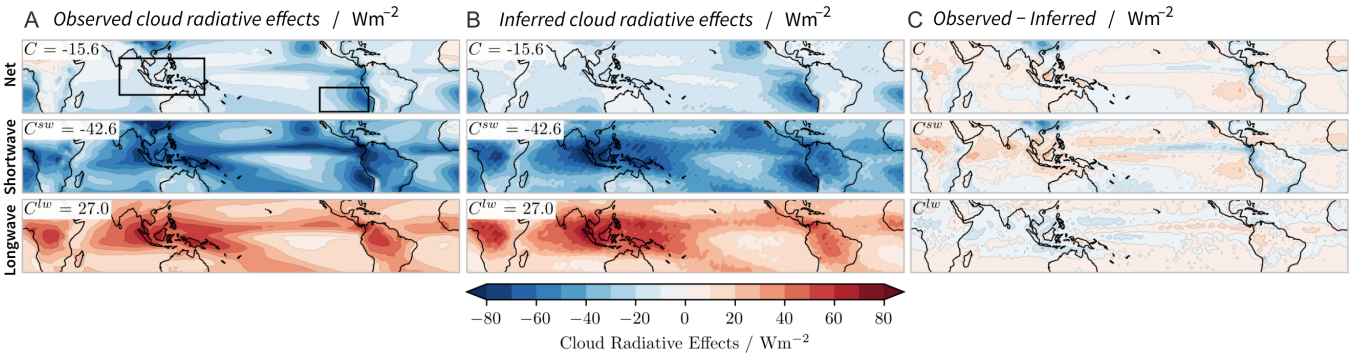

Figure 2: *Observed net, shortwave, and longwave cloud radiative effects (C, C^{sw}, C^{lw}) from CERES compared to their inferred counterparts.* Tropical mean values are shown in the upper left of each panel. The West Pacific Warm Pool and East Pacific regions are boxed in a). The colorbar is the same for all plots.

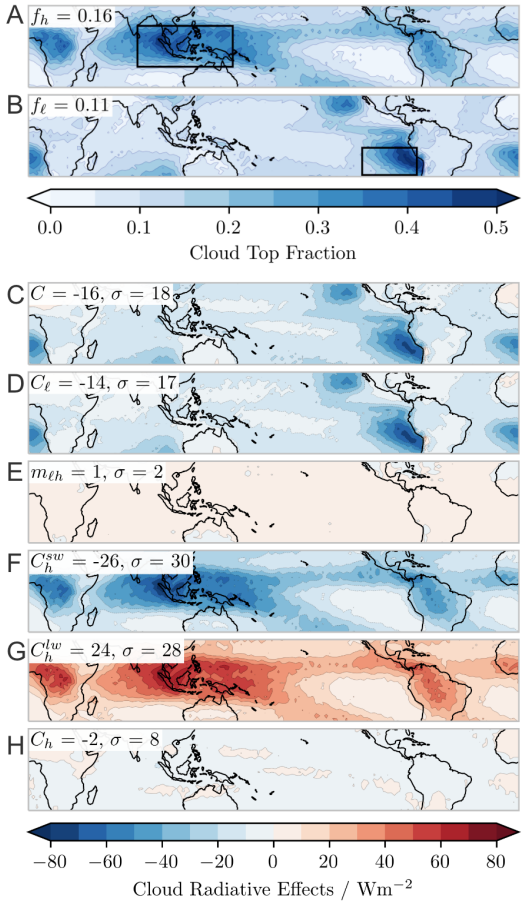

Figure 3: *Climatological values of tropical quantities.* Effective anvil cloud fraction (a) and low cloud fraction from CALIPSO (b). The West Pacific Warm Pool and East Pacific regions are boxed to indicate regions of maximum anvil and low cloud coverage, respectively. c–h) Inferred cloud radiative effects from Equations 18, 19, 21. Tropical mean values and standard deviations are shown in the upper left of each panel. Refer to Extended Data Figure 2 to see $m_{\ell h}$ and C_h plotted with a finer color scale.

and standard deviation of large-domain models in RCEMIP ($-2\pm 5\%$ K^{-1} for cloud resolving models, $-2\pm 4\%$ K^{-1} for all models, Table S5 of 40).

Now turning to ENSO-driven interannual variability, we compute annual averages of $\ln f_h$ and T_s (the tropical mean surface temperature) from July to June, similar to (22). To avoid logarithmic divergences, we exclude grid cells with $f_h = 0$. We scatter annual averages of $\ln f_h$ against T_s in Figure 4. The line of best fit for this relation gives

$$\frac{d\ln f_h}{dT_s} \approx -7 \text{ to } -11\% \text{ K}^{-1}. \quad \text{(interannual variability)} \quad (8)$$

This change is both larger than our simple estimate and from RCEMIP; it is also larger than the change of -5% K^{-1} inferred from interannual variability in AMIP runs with the IPSL, MPI, and NCAR models (see Figure S3 of 21). However, since all of these estimates of anvil cloud changes are much smaller than what is required to achieve our specified lower bound of $\langle \lambda_h^{\text{area}} \rangle = -0.4$ Wm^{-2}K^{-1}, the bounds of the area feedback can be refined.

Best estimate of the area feedback Care should be taken when determining the anvil cloud area change with warming on different timescales. Anvil area is better correlated with upper tropospheric stability than surface temperature (22, 23), and surface- and upper-tropospheric warming (and thus changes in stability) do not always go hand-in-hand on interannual timescales (41). This may alter the anvil area sensitivity to surface temperature inferred from variability. Indeed, anvil clouds are about half as sensitive for long term warming as compared to interannual variability in the IPSL general circulation model (23), the only model where such an analysis has been done. Furthermore, ENSO-driven interannual variability is not only associated with a change in surface temperature, but also a reorganization of deep convection from the West Pacific to the Central Pacific (42) which may further alter the inferred relationship between anvil area and surface temperature on different timescales.

Given the evidence from theory assuming a moist-adiabatic change in lapse rate (Equation 7), observations of interannual variability (Equation 8), and simulations (21, 23, 25), we estimate that the anvil cloud area changes at about

$$\frac{d\ln f_h}{dT_s} = -4 \pm 2\% \text{ K}^{-1}. \quad \text{(best estimate)} \quad (9)$$

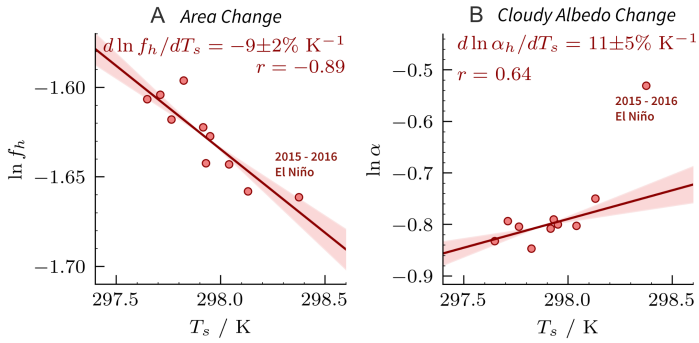

Figure 4: *Interannual changes in tropical mean anvil cloud area (a) and anvil cloud albedo (b) as a function of surface temperature.* Each point represents one year from 2006–2016. In each subplot, the slope, correlation of the best fit line and its standard error are shown. Standard error in the slope due to limited sampling is indicated by shading. In (b), the regression is calculated excluding the 2015–2016 El Niño. See Extended Data Figure 4 for regression calculated including the El Niño and the regression calculated for low cloud albedo.

We found $C_h + m_{\ell h} = -1.5\ \mathrm{Wm}^{-2}$, but other observational studies have estimated $-4\ \mathrm{Wm}^{-2}$ (38), $0.6\ \mathrm{Wm}^{-2}$ (17), and $2\ \mathrm{Wm}^{-2}$ (43). This is probably due to methodological differences and because anvil clouds have no precise definition. Furthermore, CERES TOA fluxes have their own small uncertainties (35) and considering mid-level clouds as distinct entities from low clouds adds an additional uncertainty of $0.5\ \mathrm{Wm}^{-2}$ (see Methods). Therefore, we estimate the anvil cloud radiative effect and cloud overlap effect to be,

$$C_h + m_{\ell h} = -1 \pm 3\ \mathrm{Wm}^{-2}. \quad \text{(best estimate)} \qquad (10)$$

Using these best estimates in Equation 4, we get our best estimate of the anvil area feedback to within one standard deviation:

$$\langle \lambda_h^{\text{area}} \rangle = 0.02\ \pm\ 0.07\ \mathrm{Wm}^{-2}\mathrm{K}^{-1}. \quad \text{(best estimate)} \qquad (11)$$

Overlap effects with low-level clouds are accounted for ($m_{\ell h} = 0.5\ \mathrm{Wm}^{-2}$): they dampen the anvil cloud area feedback by about 25%. Our estimate for the anvil cloud area feedback is positive but ten times smaller in magnitude and three times more constrained than the WCRP estimate of $-0.2 \pm 0.2\ \mathrm{Wm}^{-2}\mathrm{K}^{-1}$ for the anvil cloud feedback (1). We deem that the area feedback is now well constrained because its uncertainty is comparable to other cloud feedbacks (1, 2). Our results provide a theoretical and observational basis for qualitative arguments regarding a small area feedback (7, 11, 26). What about the anvil cloud albedo feedback?

Uncertainty in the anvil cloud albedo feedback

Qualitative arguments and GCM experiments suggest a significant feedback could be produced without any change in anvil area (11, 28), but let us make that notion quantitative by considering the anvil cloud albedo feedback,

$$\lambda_h^{\text{albedo}} = \frac{1}{2}\frac{d\ln \alpha_h}{dT_s}\left(C_h^{\text{sw}} + m_{\ell h}^{\text{sw}}\right). \qquad (12)$$

It follows a similar form to the area feedback but depends on the fractional change in cloud albedo with warming $d\ln\alpha_h/dT_s$, the shortwave anvil cloud radiative effect C_h^{sw}, and the shortwave cloud overlap effect $m_{\ell h}$ (see Methods for derivation).

Given that $C_h^{\text{sw}} + m_{\ell h}^{\text{sw}} \approx -25\ \mathrm{Wm}^{-2}$ (Extended Data Table 1), producing a feedback of $-0.2\ \mathrm{Wm}^{-2}\mathrm{K}^{-1}$ requires a fractional change in cloud albedo of only 1 to $2\%\ \mathrm{K}^{-1}$. In contrast to anvil area, even a small change in the anvil's cloud albedo could produce a strong radiative response. How plausible is such a change?

Changes in anvil cloud albedo with warming Computing the anvil cloud albedos for each year (see Methods), we find that $d\ln\alpha_h/dT_s \approx 6$ to $16\ \%\ \mathrm{K}^{-1}$ and significantly increases during the 2015–2016 El Niño (Figure 4b) for reasons that are unclear—anvil height and temperature are not as sensitive to El Niño (Extended Data Figure 3); and changes in low cloud albedo are more ambiguous than changes in anvil cloud albedo (Extended Data Figure 4). Taken at face value, such a change in albedo implies $\lambda_h^{\text{albedo}} \approx 1/2 \cdot 10\%\ \mathrm{K}^{-1} \cdot -25\ \mathrm{Wm}^{-2} \sim \mathcal{O}(-1)\ \mathrm{Wm}^{-2}\mathrm{K}^{-1}$, a large negative feedback. This value should be interpreted carefully.

First, it is possible that our diagnosed values of cloud albedo are biased by using an idealized two-layer model of cloud radiative effects that ignores clear-sky atmospheric absorption, assumes a spatially uniform cloud albedo, excludes the thickest ($\tau > 5$) and thinnest ($\tau < 0.3$) portions of anvil clouds, and assumes a cloud emissivity of 1. We have shown an increase in anvil cloud albedo with warming, whereas another observational study showed anvil cloud thinning with warming and thus a decrease in cloud albedo (44). Yet another observational study showed ice water path, a proxy for optical depth, to be non-monotonic with sea surface temperatures (45).

Second, there is no guarantee that long term warming will follow interannual warming, as already discussed in the context of area changes.

Third, there are no quantitative theories to understand such a change. Anvil cloud albedo might increase if anvils contain more condensate with warming, as could happen if precipitation efficiency remains constant or increases (21, 46), but the precise amount remains uncertain. It remains to be seen what happens to cloud albedo in cloud-resolving and climate models, but those results would also warrant caution because of large intermodel spreads in climatology of cloud condensate and cloud radiative effects (40).

Fourth, if the anvil cloud optical depth is increasing, then its longwave emissivity ε_h will increase too. This will produce a countervailing positive longwave feedback,

$$\lambda_h^{\text{emissivity}} = \frac{1}{2}\frac{d\ln \varepsilon_h}{dT_s}\left(C_h^{\text{lw}} + m_{\ell h}^{\text{lw}}\right), \qquad (13)$$

but with an uncertain magnitude (see Methods for further discussion).

The net result of these two competing components of the optical depth feedback are unclear, though they might be consistent with the negative anvil cloud feedback found in observations by Williams and Pierrehumbert (47) and which forms the basis of the feedback estimates in comprehensive assessments (1, 2). Given the lack of theory for understanding such changes, the conflicting observational evidence, and that there may be a countervailing longwave anvil emissivity feedback, we conclude that the magnitude and uncertainty of the anvil cloud feedback in these previous

assessments is primarily embodied by optical depth changes and not by area changes. Changes in cloud-moisture coupling and convective aggregation are not considered here, but may further impact the TOA budget (48).

Implications of uncertainty

A rigorous assessment of the anvil cloud area feedback was lacking because the confounding factors of cloud overlap and a changing cloud radiative effect on the feedback could not be accounted for. We overcame these challenges with a novel feedback decomposition and constrained the bounds on the anvil cloud area feedback by creating a physical storyline for its prior bounds and then refuting that storyline with observations and quantitative theory.

Much attention has been devoted to changes in anvil cloud area, but optical depth changes are now the most uncertain aspect of the anvil cloud response to warming. Focusing on them will therefore promise enhanced returns for constraining climate sensitivity, but doing so with observations alone will be hard because detecting cloud changes at the precision of $1\%\ \mathrm{K}^{-1}$ lie near the limit of active sensor global cloud observing systems (49).

Constraining these feedbacks will therefore require a mechanistic understanding of the partitioning of anvil clouds between its convective and stratiform components throughout its lifecyle (11, 17). Pursuing such an understanding would benefit other approaches to constraining the anvil cloud optical depth feedbacks, including emergent constraints, model inter-comparisons, cloud-controlling factor analysis, process studies, and climatological predictors, because confidence in these methods ultimately derives from understanding the physical relationships between environmental changes, cloud changes, and the TOA response.

Such a physically transparent approach has even broader implications. Communicating with the public about our confidence (or lack thereof) in clouds and climate change is hard. However, a physical theory of cloud feedbacks that can constrain, quantify, and interpret models and observations, like the one proposed here, could help clear the cloud of uncertainty.

References

[1] Sherwood, S. C. *et al.* An assessment of earth's climate sensitivity using multiple lines of evidence. *Reviews of Geophysics* **58**, e2019RG000678 (2020).

[2] Forster, P. *et al.* Chapter 7: The Earth's energy budget, climate feedbacks, and climate sensitivity. *Intergovernmenal Panel on Climate Change* (2021).

[3] Ceppi, P. & Nowack, P. Observational evidence that cloud feedback amplifies global warming. *Proceedings of the National Academy of Sciences* **118**, e2026290118 (2021).

[4] Myers, T. A. *et al.* Observational constraints on low cloud feedback reduce uncertainty of climate sensitivity. *Nature Climate Change* **11**, 501–507 (2021).

[5] Vogel, R. *et al.* Strong cloud–circulation coupling explains weak trade cumulus feedback. *Nature* **612**, 696–700 (2022).

[6] Ramanathan, V. & Collins, W. Thermodynamic regulation of ocean warming by cirrus clouds deduced from observations of the 1987 El Niño. *Nature* **351**, 27–32 (1991).

[7] Pierrehumbert, R. T. Thermostats, radiator fins, and the local runaway greenhouse. *Journal of Atmospheric Sciences* **52**, 1784 – 1806 (1995).

[8] Lindzen, R. S., Chou, M.-D. & Hou, A. Y. Does the earth have an adaptive infrared iris? *Bulletin of the American Meteorological Society* **82**, 417 – 432 (2001).

[9] Hartmann, D. L. & Michelsen, M. L. No evidence for iris. *Bulletin of the American Meteorological Society* **83**, 249 – 254 (2002).

[10] Mauritsen, T. & Stevens, B. Missing iris effect as a possible cause of muted hydrological change and high climate sensitivity in models. *Nature Geoscience* **8**, 8–13 (2015).

[11] Hartmann, D. L. Tropical anvil clouds and climate sensitivity. *Proceedings of the National Academy of Sciences* **113**, 8897–8899 (2016).

[12] Yoshimori, M., Lambert, F. H., Webb, M. J. & Andrews, T. Fixed anvil temperature feedback: Positive, zero, or negative? *Journal of Climate* **33**, 2719 – 2739 (2020).

[13] Kiehl, J. T. On the observed near cancellation between longwave and shortwave cloud forcing in tropical regions. *Journal of Climate* **7**, 559 – 565 (1994).

[14] Fu, Q., Baker, M. & Hartmann, D. L. Tropical cirrus and water vapor: an effective earth infrared iris feedback? *Atmospheric Chemistry and Physics* **2**, 31–37 (2002).

[15] Lin, B., Wielicki, B. A., Chambers, L. H., Hu, Y. & Xu, K.-M. The iris hypothesis: A negative or positive cloud feedback? *Journal of Climate* **15**, 3 – 7 (2002).

[16] Zelinka, M. D., Klein, S. A., Qin, Y. & Myers, T. A. Evaluating climate models' cloud feedbacks against expert judgment. *Journal of Geophysical Research: Atmospheres* **127**, e2021JD035198 (2022).

[17] Gasparini, B., Blossey, P. N., Hartmann, D. L., Lin, G. & Fan, J. What drives the life cycle of tropical anvil clouds? *Journal of Advances in Modeling Earth Systems* **11**, 2586–2605 (2019).

[18] Beydoun, H., Caldwell, P. M., Hannah, W. M. & Donahue, A. S. Dissecting anvil cloud response to sea surface warming. *Geophysical Research Letters* **48**, e2021GL094049 (2021).

[19] Jeevanjee, N. Three rules for the decrease of tropical convection with global warming. *Journal of Advances in Modeling Earth Systems* **14**, e2022MS003285 (2022).

[20] Zelinka, M. D. & Hartmann, D. L. Why is longwave cloud feedback positive? *Journal of Geophysical Research: Atmospheres* **115** (2010).

[21] Bony, S. *et al.* Thermodynamic control of anvil cloud amount. *Proceedings of the National Academy of Sciences* **113**, 8927–8932 (2016).

[22] Saint-Lu, M., Bony, S. & Dufresne, J.-L. Observational evidence for a stability iris effect in the tropics. *Geophysical Research Letters* **47**, e2020GL089059 (2020).

[23] Saint-Lu, M., Bony, S. & Dufresne, J.-L. Clear-sky control of anvils in response to increased CO2 or surface warming or volcanic eruptions. *npj Climate and Atmospheric Science* **5**, 78 (2022).

[24] Ito, M. & Masunaga, H. Process-level assessment of the iris effect over tropical oceans. *Geophysical Research Letters* **49**, e2022GL097997 (2022).

[25] Stauffer, C. L. & Wing, A. A. Properties, changes, and controls of deep-convecting clouds in radiative-convective equilibrium. *Journal of Advances in Modeling Earth Systems* **14**, e2021MS002917 (2022).

[26] Ceppi, P., Brient, F., Zelinka, M. D. & Hartmann, D. L. Cloud feedback mechanisms and their representation in global climate models. *WIREs Climate Change* **8**, e465 (2017).

[27] Zelinka, M. D., Klein, S. A. & Hartmann, D. L. Computing and partitioning cloud feedbacks using cloud property histograms. part ii: Attribution to changes in cloud amount, altitude, and optical depth. *Journal of Climate* **25**, 3736 – 3754 (2012).

[28] Li, R. L., Storelvmo, T., Fedorov, A. V. & Choi, Y.-S. A positive iris feedback: Insights from climate simulations with temperature-sensitive cloud–rain conversion. *Journal of Climate* **32**, 5305 – 5324 (2019).

[29] Klein, S. A., Hall, A., Norris, J. R. & Pincus, R. Low-cloud feedbacks from cloud-controlling factors: A review. *Surveys in Geophysics* **38**, 1307–1329 (2017).

[30] Stevens, B., Sherwood, S. C., Bony, S. & Webb, M. J. Prospects for narrowing bounds on earth's equilibrium climate sensitivity. *Earth's Future* **4**, 512–522 (2016).

[31] Fu, Q. & Liou, K. N. Parameterization of the radiative properties of cirrus clouds. *Journal of Atmospheric Sciences* **50**, 2008 – 2025 (1993).

[32] *Clouds and Climate: Climate Science's Greatest Challenge* (Cambridge University Press, 2020).

[33] McKim, B. A., Jeevanjee, N. & Vallis, G. K. Joint dependence of longwave feedback on surface temperature and relative humidity. *Geophysical Research Letters* **48**, e2021GL094074 (2021).

[34] Winker, D. M. *et al.* The calipso mission: A global 3d view of aerosols and clouds. *Bulletin of the American Meteorological Society* **91**, 1211 – 1230 (2010).

[35] Loeb, N. G. *et al.* Clouds and the earth's radiant energy system (ceres) energy balanced and filled (ebaf) top-of-atmosphere (toa) edition-4.0 data product. *Journal of Climate* **31**, 895 – 918 (2018).
[36] Morice, C. P. *et al.* An updated assessment of near-surface temperature change from 1850: The hadcrut5 data set. *Journal of Geophysical Research: Atmospheres* **126**, e2019JD032361 (2021).
[37] Hersbach, H. *et al.* The era5 global reanalysis. *Quarterly Journal of the Royal Meteorological Society* **146**, 1999–2049 (2020).
[38] Hartmann, D. L. & Berry, S. E. The balanced radiative effect of tropical anvil clouds. *Journal of Geophysical Research: Atmospheres* **122**, 5003–5020 (2017).
[39] Jeevanjee, N. & Romps, D. M. Mean precipitation change from a deepening troposphere. *Proceedings of the National Academy of Sciences* **115**, 11465–11470 (2018).
[40] Wing, A. A. *et al.* Clouds and convective self-aggregation in a multimodel ensemble of radiative-convective equilibrium simulations. *Journal of Advances in Modeling Earth Systems* **12**, e2020MS002138 (2020).
[41] Fueglistaler, S. Observational evidence for two modes of coupling between sea surface temperatures, tropospheric temperature profile, and shortwave cloud radiative effect in the tropics. *Geophysical Research Letters* **46**, 9890–9898 (2019).
[42] Deser, C. & Wallace, J. M. Large-scale atmospheric circulation features of warm and cold episodes in the tropical pacific. *Journal of Climate* **3**, 1254 – 1281 (1990).
[43] L'Ecuyer, T. S., Hang, Y., Matus, A. V. & Wang, Z. Reassessing the effect of cloud type on earth's energy balance in the age of active spaceborne observations. part i: Top of atmosphere and surface. *Journal of Climate* **32**, 6197 – 6217 (2019).
[44] Kubar, T. L. & Jiang, J. H. Net cloud thinning, low-level cloud diminishment, and hadley circulation weakening of precipitating clouds with tropical west pacific sst using misr and other satellite and reanalysis data. *Remote Sensing* **11** (2019).
[45] Igel, M. R., Drager, A. J. & van den Heever, S. C. A cloudsat cloud object partitioning technique and assessment and integration of deep convective anvil sensitivities to sea surface temperature. *Journal of Geophysical Research: Atmospheres* **119**, 10515–10535 (2014).
[46] Li, R. L., Studholme, J. H. P., Fedorov, A. V. & Storelvmo, T. Precipitation efficiency constraint on climate change. *Nature Climate Change* **12**, 642–648 (2022).
[47] Williams, I. N. & Pierrehumbert, R. T. Observational evidence against strongly stabilizing tropical cloud feedbacks. *Geophysical Research Letters* **44**, 1503–1510 (2017).
[48] Bony, S. *et al.* Observed modulation of the tropical radiation budget by deep convective organization and lower-tropospheric stability. *AGU Advances* **1**, e2019AV000155 (2020).
[49] Kotarba, A. Z. & Solecki, M. Uncertainty assessment of the vertically-resolved cloud amount for joint cloudsat–calipso radar–lidar observations. *Remote Sensing* .
[50] Johnson, R. H., Rickenbach, T. M., Rutledge, S. A., Ciesielski, P. E. & Schubert, W. H. Trimodal characteristics of tropical convection. *Journal of Climate* **12**, 2397 – 2418 (1999).
[51] Coakley, J. A. & Baldwin, D. G. Towards the objective analysis of clouds from satellite imagery data. *Journal of Applied Meteorology and Climatology* **23**, 1065 – 1099 (1984).
[52] Oreopoulos, L., Cho, N. & Lee, D. Revisiting cloud overlap with a merged dataset of liquid and ice cloud extinction from cloudsat and calipso. *Frontiers in Remote Sensing* **3** (2022).
[53] Koll, D. D. B. & Cronin, T. W. Earth’s outgoing longwave radiation linear due to h¡sub¿2¡/sub¿o greenhouse effect. *Proceedings of the National Academy of Sciences* **115**, 10293–10298 (2018).
[54] Held, I. M. & Shell, K. M. Using relative humidity as a state variable in climate feedback analysis. *Journal of Climate* **25**, 2578 – 2582 (2012).
[55] Zelinka, M. D. *et al.* Causes of higher climate sensitivity in cmip6 models. *Geophysical Research Letters* **47**, e2019GL085782 (2020).
[56] Flanner, M. G., Shell, K. M., Barlage, M., Perovich, D. K. & Tschudi, M. A. Radiative forcing and albedo feedback from the Northern Hemisphere cryosphere between 1979 and 2008. *Nature Geoscience* **4**, 151–155 (2011).
[57] Thompson, D. W. J., Bony, S. & Li, Y. Thermodynamic constraint on the depth of the global tropospheric circulation. *Proceedings of the National Academy of Sciences* **114**, 8181–8186 (2017).
[58] Loeb, N. G. *et al.* Toward a consistent definition between satellite and model clear-sky radiative fluxes. *Journal of Climate* **33**, 61 – 75 (2020).
[59] Chen, T. S. & Ohring, G. On the relationship between clear-sky planetary and surfae albedos. *Journal of Atmospheric Sciences* **41**, 156 – 158 (1984).
[60] NASA/LARC/SD/ASDC. Calipso lidar level 3 cloud occurrence data, standard v1-00 (2018).

Corresponding Author

Correspondence should be addressed to Brett A. McKim at bam218@exeter.a

Acknowledgements

We thank Geet George for illustrating the clouds in Figure 1, and Adam Sokol, Dennis Hartmann, Marion Saint-Lu, Blaž Gasparini, Isla Simpson, David Randall, and Bjorn Stevens for helpful conversations. We also thank Stephen Klein and two other anonymous reviewers whose comments have greatly improved this paper. B.M. was supported by the Franco-American Fulbright Commission. S.B. and J.L.D. were supported by EU Horizon 2020 grant agreement 820829 (CONSTRAIN).

Author Contributions

B.A.M and S.B. designed research; B.A.M. performed research. B.A.M, S.B, and J.L.D. analyzed data; and B.A.M wrote the paper.

Methods

Data availability CERES data were obtained from the NASA Langley Research Center (https://ceres.larc.nasa.gov/data/). CALIPSO / CLOUDSAT data were obtained from NASA Atmospheric Science Data Center (https://asdc.larc.nasa.gov/project/CALIPSO/CAL_LID_L3_Cloud_Occurrence-Standard-V1-00_V1-00). ERA5 reanalysis data were obtained from the Copernicus Climate Change Service (https://cds.climate.copernicus.eu/). HadCRUT5 data were obtained from the Met Office Hadley Centre (https://www.metoffice.gov.uk/hadobs/hadcrut5/data/current/download.html).

Code availability All scripts used to support the analysis of satellite and reanalysis data will be made available in a Github repository upon acceptance.

Conceptualizing cloud radiative effects We start with an idealized model of cloud radiative effects at the top of the atmosphere (TOA). Although tropical cloudiness is expected to be trimodal (50), for simplicity we will consider a domain containing two cloud types: high clouds (h) and low clouds (ℓ). (Many assessments of cloud feedbacks also use this bi-modal decomposition (1).) Each type has an emission temperature T_h, T_ℓ; an optically thick cloud fraction f_h, f_ℓ; and an albedo α_h, α_ℓ (Figure 1). Mid-level clouds will be considered in our error analysis.

The TOA energy balance is $N = S - R$, where S is the absorbed shortwave radiation and R is the outgoing longwave radiation. The cloud radiative effect C is the difference in N between all-sky and clear-sky (cs) conditions, $C = N - N_{\text{cs}}$ (51). C can be decomposed into longwave and shortwave components: $C = C^{\text{sw}} + C^{\text{lw}}$.

In the longwave component, clear-sky regions with a surface temperature T_s will emit to space with an outgoing longwave radiation of $R_{\text{cs}}^{T_s}$, but a portion will be blocked by clouds. Longwave emissivity will not be considered because most clouds have an emissivity close to one (31). Assuming random overlap between high clouds and low clouds (52), the domain-averaged clear-sky contribution is $R_{\text{cs}}^{T_s}(1-f_h)(1-f_\ell)$. Low clouds are so close to the surface that we treat their emission to space like clear-sky surface emission but at T_ℓ. Their domain-averaged contribution is $R_{\text{cs}}^{T_\ell} f_\ell (1-f_h)$. Since $R_{\text{cs}}^{T_s}$ is an approximately linear function of temperature (53), $R_{\text{cs}}^{T_\ell} \approx R_{\text{cs}}^{T_s} + \lambda_{\text{cs}}(T_s - T_\ell)$, where $\lambda_{\text{cs}} \equiv -dR_{\text{cs}}/dT_s \approx -2$ Wm^{-2}K^{-1} is a representative value for the longwave clear sky feedback (33). We assume that high clouds are so high that they emit directly to space (32) with a value $\sigma T_h^4 f_h$. Summing these contributions, the domain-averaged outgoing longwave radiation is

$$R = R_{\text{cs}}^{T_s}(1-f_h) + \sigma T_h^4 f_h + \lambda_{\text{cs}}(T_s - T_\ell)(1-f_h)f_\ell, \tag{14}$$

and the longwave cloud radiative effect $-(R - R_{\text{cs}})$ is

$$C^{\text{lw}} = R_{\text{cs}}^{T_s} f_h - \sigma T_h^4 f_h - \lambda_{\text{cs}}(T_s - T_\ell)(1-f_h)f_\ell. \tag{15}$$

In the shortwave component, there is an incoming solar radiation $S^{\downarrow}$, and we assume that there is no absorption except at the surface. High clouds reflect a portion $\alpha_h f_h$ back to space. The transmitted radiation then hits low clouds which reflect a portion $\alpha_\ell f_\ell$ back to space (ignoring secondary reflections with the anvils above). The transmitted radiation then hits the surface which reflects a portion α_s back out to space and absorbs the rest. Summing these contributions, the domain-averaged absorbed shortwave radiation at TOA is

$$S = S^{\downarrow}(1-\alpha_h f_h)(1-\alpha_\ell f_\ell)(1-\alpha_s). \tag{16}$$

The TOA absorbed shortwave in clear-skies is $S_{\text{cs}} = S^{\downarrow}(1-\alpha_s)$, so the shortwave cloud radiative effect $(S - S_{\text{cs}})$ is:

$$C^{\text{sw}} = S_{\text{cs}}\big(-\alpha_h f_h - \alpha_\ell f_\ell + \alpha_h \alpha_\ell f_h f_\ell\big). \tag{17}$$

It will prove helpful to separate the contribution of isolated high clouds and isolated low clouds to the net cloud radiative C. Setting $f_\ell = 0$ yields the isolated high cloud radiative effect:

$$C_h = \big(-S_{\text{cs}}\alpha_h + R_{\text{cs}}^{T_s} - \sigma T_h^4\big) f_h. \tag{18}$$

Setting $f_h = 0$ yields the isolated low cloud radiative effect:

$$C_\ell = \big(-S_{\text{cs}}\alpha_\ell - \lambda_{\text{cs}}(T_s - T_\ell)\big) f_\ell. \tag{19}$$

The total cloud radiative effect C in terms of each cloud is:

$$C = C_h + C_\ell + m_{\ell h}, \tag{20}$$

where

$$m_{\ell h} = \big(S_{\text{cs}}\alpha_\ell\alpha_h + \lambda_{\text{cs}}(T_s - T_\ell)\big) f_\ell f_h, \tag{21}$$

represents the cloud overlap masking effect. Note that $C_h \propto f_h, C_\ell \propto f_\ell$, and $m_{\ell h} \propto f_\ell f_h$.

Feedback decomposition We will now derive various cloud feedbacks from these equations and assume a fixed relative humidity. The lapse rate feedback has been shown to be small when using this reference response (54, 55), so it will be ignored here.

$$\begin{aligned}
\lambda &\equiv \frac{dN}{dT_s} \\
&= \frac{S_{\text{cs}}}{dT_s} - \frac{dR_{\text{cs}}^{T_s}}{dT_s} + \frac{dC}{dT_s} \\
&= \lambda_{\text{cs}}(1-f_h) \\
&\quad + (R_{\text{cs}}^{T_s} - \sigma T_h^4 + \lambda_{\text{cs}}(T_s - T_\ell)f_\ell - S_{\text{cs}}\alpha_h + S_{\text{cs}}\alpha_h\alpha_\ell f_\ell)\frac{df_h}{dT_s} \\
&\quad + (-\lambda_{\text{cs}}(T_s - T_\ell)(1-f_h) - S_{\text{cs}}\alpha_\ell + S_{\text{cs}}\alpha_h f_h \alpha_\ell)\frac{df_\ell}{dT_s} \\
&\quad + -4\sigma T_h^3 f_h \frac{dT_h}{dT_s} \\
&\quad + -\lambda_{\text{cs}}(1-f_h)f_\ell \frac{d(T_s - T_\ell)}{dT_s} \\
&\quad + (-S_{\text{cs}} f_h + S_{\text{cs}} f_h \alpha_\ell f_\ell)\frac{d\alpha_h}{dT_s} \\
&\quad + (-S_{\text{cs}} f_\ell + S_{\text{cs}}\alpha_h f_h f_\ell)\frac{d\alpha_\ell}{dT_s} \\
&\quad - S^{\downarrow}(1-\alpha_h f_h)(1-\alpha_\ell f_\ell)\frac{d\alpha_s}{dT_s} \\
&\quad - (T_s - T_\ell)(1-f_h)f_\ell \frac{d\lambda_{\text{cs}}}{dT_s}.
\end{aligned} \tag{22}$$

Recognizing that many of these terms can be rewritten as cloud radiative effects, we get:

$$
\begin{aligned}
\lambda = \lambda_{\text{cs}}(1-f_h) \\
&+ \left(C_h + m_{\ell h}\right)\frac{d\ln f_h}{dT_s} \\
&+ \left(C_\ell + m_{\ell h}\right)\frac{d\ln f_\ell}{dT_s} \\
&- 4\sigma T_h^3 f_h \frac{dT_h}{dT_s} \\
&- \lambda_{\text{cs}}(1-f_h) f_\ell \frac{d(T_s - T_\ell)}{dT_s} \\
&+ \left(C_h^{\text{sw}} + m_{\ell h}^{\text{sw}}\right)\frac{d\ln \alpha_h}{dT_s} \\
&+ \left(C_\ell^{\text{sw}} + m_{\ell h}^{\text{sw}}\right)\frac{d\ln \alpha_\ell}{dT_s} \\
&+ C_s \frac{d\ln \alpha_s}{dT_s},
\end{aligned}
\tag{23}
$$

where we have assumed that $d\lambda_{\text{cs}}/dT_s$ is negligible, and $C_s = -S^{\downarrow}(1-\alpha_h f_h)(1-\alpha_\ell)\alpha_s$ is the surface albedo radiative effect, which is equivalent to the "cryosphere radiative forcing" (56).

Now we name and then describe each term:

$$
\lambda = \lambda_0 + \lambda_h^{\text{area}} + \lambda_\ell^{\text{area}} + \lambda_h^{\text{temp}} + \lambda_\ell^{\text{temp}} + \lambda_h^{\text{albedo}} + \lambda_\ell^{\text{albedo}} + \lambda_s^{\text{albedo}} \tag{24}
$$

λ_0 is the anvil cloud-masked longwave clear-sky feedback. It is our null hypothesis for the climate response to warming because it assumes fixed relative humidity; fixed anvil temperature, area, and albedo; fixed low cloud temperature difference, area, and albedo; and fixed surface albedo. λ_h^{area} and $\lambda_\ell^{\text{area}}$ are the feedbacks from a changing anvil cloud and low cloud area, respectively. λ_h^{temp} is the feedback from a changing anvil cloud temperature. $\lambda_\ell^{\text{temp}}$ is the feedback from a changing temperature difference between low clouds and the surface. $\lambda_h^{\text{albedo}}$, $\lambda_\ell^{\text{albedo}}$, and $\lambda_s^{\text{albedo}}$ are the feedbacks from a changing albedo of anvil clouds, low clouds, and surface, respectively. We omit the surface albedo feedback from Equation 2 because we are interested in tropical climate.

For simplicity, we have assumed that cloud emissivities of high clouds and low clouds $(\varepsilon_h, \varepsilon_\ell)$ are equal to one (31). However, if we relax this assumption for completeness, one can show this leads to a high- and low-cloud emissivity feedback with the following form:

$$
\begin{aligned}
\lambda_h^{\text{emissivity}} &= \left(C_h^{\text{lw}} + m_{\ell h}^{\text{lw}}\right)\frac{d\ln \varepsilon_h}{dT_s}, \\
\lambda_\ell^{\text{emissivity}} &= \left(C_\ell^{\text{lw}} + m_{\ell h}^{\text{lw}}\right)\frac{d\ln \varepsilon_\ell}{dT_s},
\end{aligned}
\tag{25}
$$

which closely resemble the form of the cloud albedo feedback. Some of the other feedbacks will have small modifications, but they are unimportant here.

Climatology We combine monthly-mean satellite observations, surface temperature measurements, and reanalysis and re-grid all datasets onto a common 2° latitude × 2.5° longitude grid over the tropical belt (30°N−30°S) from June 2006 to December 2016. Although anvil clouds populate the globe (57), it is less clear how extratropical anvils change with warming. Most cloud feedback assessments only consider tropical anvil clouds, so we will follow this convention.

From the CALIPSO lidar satellite dataset (34), we obtain vertical profiles of cloud fraction for optical depths between $0.3 \leq \tau \leq 5$. This range excludes both deep convective cores and optically thin cirrus unconnected to deep convection (22). We then vertically smooth the native vertical 60 m resolution profiles with a 480 m running mean. For anvil detection, we consider ice cloud data above 8 km. For shallower clouds, we consider the sum of ice and liquid cloud fraction data below 8 km. The diagnosed cloud fractions are the absolute maximum of the profile in their respective domains, but if the identified maximum does not exceed a cutoff ($f_{\text{cut}} = 0.03$), then that region is considered to be clear-sky ($f = 0$). This algorithm is applied to every grid point and then tropically-averaged. Our approach thus far resembles (22), just extended to include low clouds.

To match the inferred cloud radiative effects with the observed, we consider an effective cloud fraction $f_h = n \cdot \text{Max}(f(z))$ for high clouds, where n is a single tuned parameter to account for collapsing the high cloud profile into one level. This accounting is more important for high clouds, as their profile's full width-half maximum is ≈ 5 km (Figure 1 of Extended Data), whereas low clouds are already localized with a full width-half maximum of ≈ 1 km (Figure 1 of Extended Data). While n could be more rigorously derived from detailed considerations of cloud overlap (52), we opt to determine n by fitting the predicted tropical- and time-averaged longwave cloud radiative effect C^{lw} to its observed counterpart $C_{\text{obs}}^{\text{lw}}$ from CERES (see **Cloud fraction** section of Methods). Doing so yields a spatially and temporally constant value of $n = 1.7$. This value lies between that from assuming maximum overlap between each layer of the anvil cloud, which yields $n = 1$ and random overlap, which yields $n \approx 5$.

The height of the diagnosed cloud fraction is then used to diagnose the cloud temperatures T_h, T_ℓ at each space and time by selecting the corresponding atmospheric temperature in ERA5 reanalysis (37). We use the HadCRUT5 dataset (36) to diagnose the surface temperature T_s.

We use monthly mean TOA radiative fluxes, both clear-sky and all-sky, from the CERES satellite EBAF Ed4.1 product (35, 58). We diagnose the surface albedo α_s as the ratio of upwelling clear-sky shortwave radiation $S_{\text{cs}}^{\uparrow}$ to incoming shortwave radiation $S^{\downarrow}$. However, because shortwave absorption and scattering occurs in the real atmosphere, our surface albedo is more accurately characterized as the planetary clear-sky albedo (59). We diagnose the cloud albedos by assuming that they are constant in space, and by fitting the predicted tropical- and time-averaged shortwave cloud radiative effect C^{sw} to its observed counterpart $C_{\text{obs}}^{\text{sw}}$ from CERES. With two unknowns we must provide two constraints. We do this by splitting the tropics into two distinct dynamical regimes based on threshold of 500 hPa midtropospheric velocity $\omega_{500} = 25$ hPa day^{-1} obtained from monthly ERA5 reanalysis data. These regions are treated as independent so that they provide two constraints. The regime-averaged shortwave radiative effect is then fitted to its observed counterpart by using the `fsolve` function from the `scipy.optimize` python module. (The precise threshold of 25 hPa day^{-1} was chosen because it resulted in the smallest root mean square error between C^{sw} and $C_{\text{obs}}^{\text{sw}}$.)

Cloud fraction We use the CALIPSO Lidar Satellite CAL_LID_L3_Cloud_Occurence-Standard-V1-00 data product (60), the same dataset used in (22). While the high cloud fraction could simply be diagnosed as the maximum cloud fraction of the profile (i.e. $f_h = \text{Max}(f(z))$), the calculated longwave cloud radiative effect C^{lw} will not match with observations. To rectify this, we will consider using a single tuning parameter, n. That is, we have an effective cloud fraction $f_h = n \cdot \text{Max}(f(z))$ which accounts for representing a cloud profile with a single level.

We first demand that n be constant with space and time to ensure that areal changes (changes in f_h) are not artificially convolved with vertical changes which relate to optical depth and albedo (α). This decision projects the spatio-temporal variability in the vertical extent of anvils more onto α than f_h.

We then fit the predicted tropically- and temporally-averaged longwave radiative effect C^{lw} to its observed counterpart $C_{\text{obs}}^{\text{lw}}$ from CERES. Given these constraints, and the inputs to Equation 15, n can be solved for as

$$n = \frac{\langle C_{\text{obs}}^{\text{lw}} + \lambda_{\text{cs}}(T_s - T_\ell) f_\ell \rangle}{\langle R_{\text{cs}} \max(f(z)) - \sigma T_h^4 \max(f(z)) + \lambda_{\text{cs}}(T_s - T_\ell) f_\ell \max(f(z)) \rangle}, \tag{26}$$

where $\langle \cdot \rangle$ denotes a tropical- and temporal-average.

Uncertainty analysis for area feedback Uncertainty in our estimates of $d \ln f_h / dT_s$ and $C_h + m_{\ell h}$ translate to uncertainty in λ_h^{area}. As stated in the main text, we estimate $d \ln f_h / dT_s = -4 \pm 2$ % K^{-1}. For the anvil cloud radiative effect, we found $C_h + m_{\ell h} = -1.5$ Wm^{-2}. However, other observational studies have found it to be -4 Wm^{-2} (38), 0.6 Wm^{-2} (17), and 2 Wm^{-2} (43). This is probably due to methodological differences and the fact that anvil clouds have no precise definition. Furthermore, CERES TOA fluxes monthly fluxes have a stated uncertainty of 2.5 Wm^{-2} (35).

Another source of error comes from neglecting mid-level clouds, a fairly common cloud type (50), as their own identities. Let's assume that emission from mid level congestus clouds (c) experience a clear-sky greenhouse effect. By symmetry with low clouds, they should contribute an additional cloud overlap masking term that appears in our expression for λ_{area}: $m_{ch} = (S_{\text{cs}} \alpha_c \alpha_h + \lambda_{\text{cs}}(T_s - T_c)) f_c f_h$. Assuming that $f_c = 0.1$, $f_h = 0.17$, $\alpha_c = \alpha_h = 0.45$, $T_c = 250$ K, $T_s = 298$ K, $S_{\text{cs}} = 347$ Wm^{-2}, $\lambda_{\text{cs}} = -2$ Wm^{-1}K^{-1} yields $m_{ch} \approx -0.5$ Wm^{-2}.

We therefore estimate $C_h + m_{\ell h} = -1 \pm 3$ Wm^{-2}. This results in our best estimate of the anvil cloud area feedback:

$$\begin{aligned} \langle \lambda_h^{\text{area}} \rangle &= 1/2 \cdot (-4 \pm 2 \text{ \% K}^{-1}) \cdot (-1 \pm 3 \text{ Wm}^{-2}) \\ &= 0.02 \pm 0.07 \text{ Wm}^{-2}\text{K}^{-1}. \end{aligned} \tag{27}$$

Further uses of our framework Our feedback expressions might also provide a quick, quantitative, and physically transparent way to interpret how model biases influence feedbacks. For instance, if members of a GCM ensemble simulate C_h between ± 10 Wm^{-2}, but they all simulate the same $d \ln f_h / dT_s = -4\%$ K^{-1}, then their area feedbacks will range between ∓ 0.2 Wm^{-2}K^{-1}. If all ensemble members simulate $C_h = 1$ Wm^{-2}, but simulate $d \ln f_h / dT_s = \pm 5\%$ K^{-1}, then their area feedbacks will range between ± 0.03 Wm^{-2}K^{-1}. This quantitative yet clear diagnostic could provide testable hypothesis that advance our understanding and development of models.

Extended Data

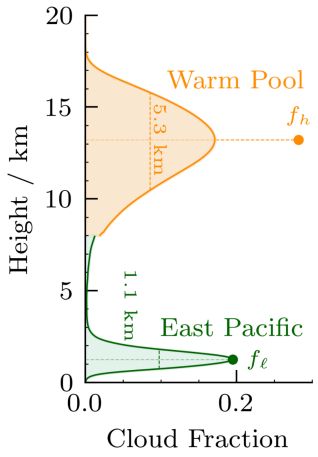

Extended Data Figure 1: *Illustration of effective cloud fraction.* The high cloud fraction profile in the Warm Pool and low cloud fraction profile in the East Pacific are from CALIPSO. The full width-half maximum and effective cloud fraction of each profile are shown. The high cloud and low cloud profiles are clipped below 8 km and above 4 km, respectively, in accordance with our detection method.

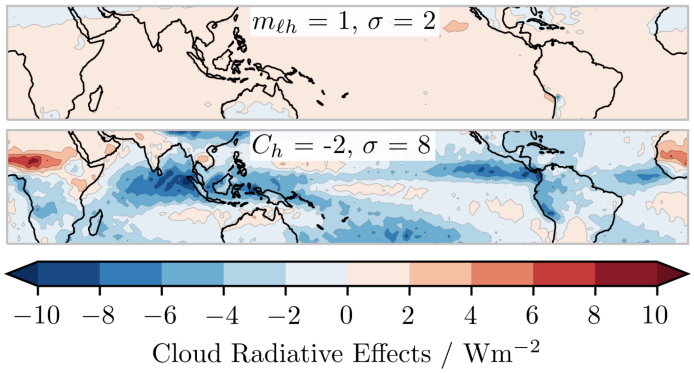

Extended Data Figure 2: *Climatological values of tropical quantities.* Top) Inferred cloud overlap effect from Equation 21. Bottom) Inferred anvil cloud radiative effect from Equation 18. Tropical mean values and standard deviations are shown in the upper middle of each panel. Refer to Figure 3 to see $m_{\ell h}$ and C_h and other quantities plotted with a broader color scale.

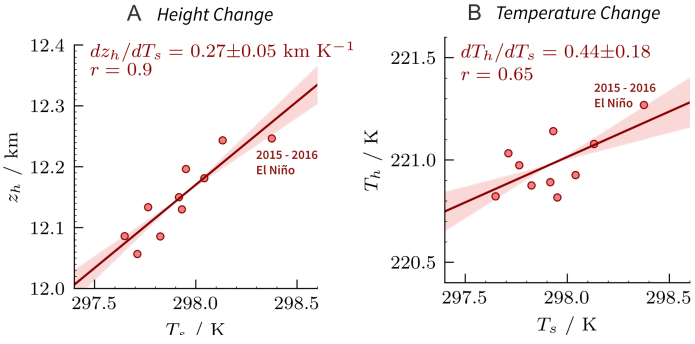

Extended Data Figure 3: *Interannual changes in tropical mean anvil cloud height (a) and temperature (b).* In each subplot, the slope, correlation for the best fit line and its standard error are shown. Standard error in the slope due to limited sampling is indicated by shading.

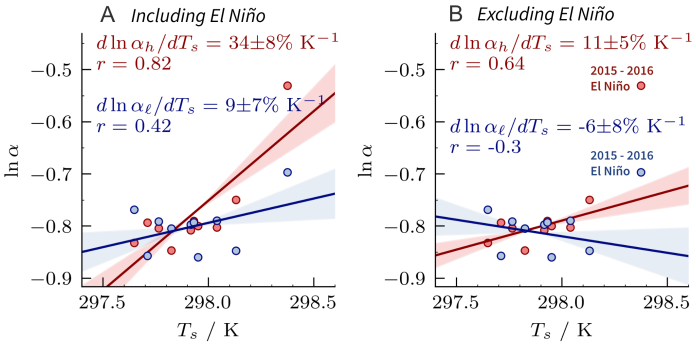

Extended Data Figure 4: *Interannual changes in tropical mean anvil cloud albedo (red) and low cloud albedo (blue).* (a) The line of best fit is calculated with the 2015–2016 El Niño included. (b) The line of best of fit is calculated without the El Niño.

Extended Data Table 1: *Climatological values of tropical quantities (30°S – 30°N) used in this study.* All radiative quantities are evaluated at the top of atmosphere. $C^{\text{lw}}_{\text{obs}}$ and $C^{\text{sw}}_{\text{obs}}$ refer to the observed longwave and shortwave cloud radiative effects from CERES. See Climatology section for details.

Quantity	Description	Tropical mean value	Derivation
f_h	Anvil cloud area fraction	0.16	CALIPSO
f_ℓ	Low cloud area fraction	0.11	CALIPSO
T_h	Anvil temperature	221 K	ERA5
T_ℓ	Low cloud temperature	287 K	ERA5
T_s	Surface temperature	298 K	HadCRUT5
α_s	Planetary surface albedo	0.13	CERES
$S^{\downarrow}$	Incoming shortwave radiation	398 Wm^{-2}	CERES
S_{cs}	Clear-sky absorbed shortwave	347 Wm^{-2}	CERES
R_{cs}	Clear-sky outgoing longwave	287 Wm^{-2}	CERES
n	Effective cloud fraction scaling	1.7	Fitted from $C^{\text{lw}}_{\text{obs}}$
α_h	Anvil albedo	0.45	Fitted from $C^{\text{sw}}_{\text{obs}}$
α_ℓ	Low cloud albedo	0.45	Fitted from $C^{\text{sw}}_{\text{obs}}$
C	Net cloud radiative effect	-15.6 Wm^{-2}	Inferred
C^{sw}	Shortwave cloud radiative effect	-42.6 Wm^{-2}	Inferred
C^{lw}	Longwave cloud radiative effect	27.0 Wm^{-2}	Inferred
C_h	Anvil cloud radiative effect	-2.0 Wm^{-2}	Inferred
C^{sw}_h	Shortwave anvil cloud radiative effect	-26.1 Wm^{-2}	Inferred
C^{lw}_h	Longwave anvil cloud radiative effect	24.1 Wm^{-2}	Inferred
C_ℓ	Low cloud radiative effect	-14.3 Wm^{-2}	Inferred
C^{sw}_ℓ	Shortwave low cloud radiative effect	-17.3 Wm^{-2}	Inferred
C^{lw}_ℓ	Longwave low cloud radiative effect	3.1 Wm^{-2}	Inferred
$m_{\ell h}$	Cloud overlap effect	0.6 Wm^{-2}	Inferred
$m^{\text{sw}}_{\ell h}$	Shortwave cloud overlap effect	1.1 Wm^{-2}	Inferred
$m^{\text{lw}}_{\ell h}$	Longwave cloud overlap effect	-0.5 Wm^{-2}	Inferred